AIAA JOURNAL
Vol. 48, No. 10, October 2010

Nonlinear Model Reduction of von Kármán Plates Under Quasi-Steady Fluid Flow

M. R. Brake* and D. J. Segalman
Sandia National Laboratories, Albuquerque, New Mexico 87185

DOI: 10.2514/1.J050357

A reduced-order model for von Kármán plates, using a method of quadratic components, is presented in this paper. The method of quadratic components postulates the full kinematics of the plate as consisting of a combination of linear and quadratic components. This reduced model is then discretized in space with a Galerkin approximation and in time with an implicit integration scheme. The plate is coupled with a fluid flowing over it at a supersonic speed using a quasi-steady pressure model commonly referred to as piston theory. A static loading example is used to validate the model reduction of the plate with respect to other numerical and approximate solutions. The limit cycles of the plate coupled with piston theory are calculated via a cyclic method, and the results from parameter studies are compared to classical results. A previously unexplored regime of the limit cycle amplitudes is investigated; a second, coexisting, limit cycle is found that yields a discontinuity in the limit cycle amplitudes at a critical dynamic pressure.

Nomenclature

c, c_0	=	normalization coefficients for the reduced-order and one-term models
$\mathcal{D}$	=	flexural stiffness of the plate
E	=	modulus of elasticity of the plate
$\underline{f}$, f_n	=	vector of applied forces for the expansion method and the nth applied force
G_n	=	applied force for the nth degrees of freedom in the Galerkin discretization
$\underline{G}_{nm}$	=	nmth quadratic basis function for the reduced model
g	=	applied external load
h	=	thickness of the plate
$\mathbb{I}$	=	identity matrix
$\underline{i}$, $\underline{j}$, $\underline{k}$	=	unit normal vectors in the x, y, and z directions
$\mathbb{K}$	=	stiffness matrix
K	=	stiffness of the linear plate
L_x, L_y	=	plate length in the flow direction and the cross-stream direction
$\mathbb{M}$	=	mass matrix
M	=	Mach number
m, n, r, s	=	indices for the expansion terms
$\underline{\mathcal{N}}$	=	response of the full model
N	=	number of expansion terms
$\mathbb{P}_{nm}$	=	matrix of cubic stiffness terms for the nmth degree of freedom
P_{srnm}	=	cubic stiffness term for the $srnm$th degree of freedom
p, p_∞	=	fluid pressure acting on the plate and in the far field
R	=	residual error for an implicit integration time step
T	=	limit cycle period
t	=	time
U, V, W	=	reduced-order model bases for the displacements in x, y, and z
u, v, w	=	plate displacement in the x, y, and z directions
$\underline{\mathcal{W}}$	=	postulated solution to the nonlinear equations
x	=	direction of the fluid flow (in-plane)
$\underline{Y}_n$	=	nth linear basis function for the reduced model
y	=	in-plane direction orthogonal to the fluid flow
z	=	out-of plane direction
$\underline{\alpha}$, α_n	=	vector of expansion coefficients and the nth expansion coefficient
β, γ	=	implicit integration coefficients determined from λ
ε_{ij}	=	ij component of the internal strain
ε_u	=	strain due to the longitudinal deformation for the one-term approximation
ε_w	=	longitudinal strain due to lateral deformation for the one-term approximation
$\underline{\zeta}$, ζ_n	=	first time derivative of $\underline{\alpha}$ and α_n
λ	=	implicit integration coefficient
λ^*	=	nondimensional dynamic pressure
μ	=	speed of sound in the fluid
ν	=	Poisson ratio of the plate
$\underline{\xi}$, ξ_n	=	second time derivative of $\underline{\alpha}$ and α_n
ρ	=	density of the plate
ρ_f	=	density of the fluid
τ	=	nondimensionalized period
Υ	=	fluid velocity
$\underline{\phi}_n$	=	nth basis function
$\underline{\chi}$	=	estimation of the expansion coefficients at the next time step
Ψ	=	maximum limit cycle amplitude at $x = 3/4L_x$ and $y = 1/2L_y$
ψ_n	=	limit cycle amplitude for the nth degree of freedom
Ω_n	=	nth natural frequency of the linearized plate
ω_n^2	=	stiffness for the nth degree of freedom in the Galerkin discretization

I. Introduction

AS ENGINEERING structures become more complex, the computational analysis of high fidelity models based on the full structure becomes prohibitively expensive. Techniques to reduce the number of degrees of freedom of the models, while preserving all of the relevant physics, are needed in order to analyze and optimize the design of complex structures. One approach of model reduction methods for structures is to first develop a full finite element model, then use a component mode synthesis approach to significantly reduce the number of degrees of freedom while incorporating the essential physics of the system including the nonlinearities [1–4]. Other approaches include the use of a Galerkin approximation based on the results of a finite element analysis [5] or a hierarchical finite element method in which the order of the approximating polynomial is increased, while the mesh size is held constant, which allows for

Received 10 December 2009; revision received 17 May 2010; accepted for publication 29 May 2010.

*P.O. Box 5800, MS 0346; mrbrake@sandia.gov (Corresponding Author).

meshes with as little as one element for a plate [6,7]. These methods, however, can not be applied directly to nonlinear problems.

The von Kármán plate theory considers a class of nonlinear plates that takes into account in-plane stretching (a membrane nonlinearity) in the equations of motion and thus allows for the modeling of large displacements of the plate. A modal expansion solution exists for the case of a cantilevered von Kármán plate [8], but analytical closed-form solutions are not available for most other cases with general boundary conditions. A number of approximate methods exist, however, that can accurately model von Kármán plates and shells [9]. Approximate methods include finite elements, both spline finite strip methods [10] and hierarchical finite element methods [6,7], nonlinear normal modes [11], and assumed displacement fields with Taylor series expansions in the normal directions [12]. The present paper seeks to develop a more efficient method in order to make the analysis of complex problems more practical.

In what follows, von Kármán plate theory is employed to model the structure considered here, a panel on an aircraft or other moving body. The von Kármán plate is coupled to an adjacent supersonic flow via a quasi-steady aerodynamic theory commonly referred to as piston theory. Dowell [13] considered the same problem and used a Galerkin approximation to model the mode shapes of the plate, while introducing an additional basis for the membrane motion that was coupled nonlinearly to the mode shapes through a weighted residuals technique. Other related aeroelastic problems include the use of a cylindrical bending assumptions for the plate [13–15], which effectively reduce the problem to that of a beam, and panels in crossflows subjected to thermal and acoustic loads [16,17].

In the present work, the von Kármán plate equations are presented in Sec. II and are discretized using the method of quadratic components in Sec. II.A. The advantage of this method is that there will only be as many degrees of freedom as there are bending modes, which is significantly fewer degrees of freedom than alternative approaches. A Galerkin method is then applied in Sec. II.B to develop an equation of motion in terms of the modal coefficients, and an implicit integration scheme for solving the coupled, nonlinear differential equations developed in the Galerkin discretization is presented in Sec. II.C. An example to validate the discretization of the plate's equation of motion is presented in Sec. II.D in order to compare the results from an explicit closed-form solution for the linear plate to a one-term approximation of the nonlinear plate, a numerical analysis of the nonlinear plate performed in ABAQUS, and the present method with five mode shapes for the nonlinear plate. Finally, in Sec. III, the coupling of the discretized plate with piston theory is presented. A cyclic method for calculating the limit cycle amplitudes is described, and a comparison to the results of [13,16–18] is made. A previously unexplored regime of the limit cycles is explored in which a second, coexisting limit cycle is shown to cause a discontinuity in the limit cycle amplitude due to a snap-through transition from one limit cycle to the next.

II. Von Kármán Plate

For thin plates, the out-of-plane displacement w is a function of the planar coordinates $w(x, y, z, t) = w(x, y, t)$ (where x is the direction of the fluid flow and y is the in-plane direction orthogonal to the flow) and time t. The plate has length and width L_x and L_y in the x and y directions. With the Kirchhoff assumption [19], the internal strains are

$$\varepsilon_{xx} = \frac{\partial u}{\partial x} + \frac{1}{2}\left(\frac{\partial w}{\partial x}\right)^2 \tag{1}$$

$$\varepsilon_{yy} = \frac{\partial v}{\partial y} + \frac{1}{2}\left(\frac{\partial w}{\partial y}\right)^2 \tag{2}$$

$$\varepsilon_{xy} = \frac{1}{2}\left(\frac{\partial v}{\partial x} + \frac{\partial u}{\partial y} + \frac{\partial w}{\partial x}\frac{\partial w}{\partial y}\right) \tag{3}$$

Following [19], the equations of motion for a thin plate with a membrane nonlinearity and thickness h can be written in terms of the strains as

$$\rho h w_{,tt} + \mathcal{D}\nabla^4 w = g + \frac{12\mathcal{D}}{h^2}\left((\varepsilon_{xx} + \nu\varepsilon_{yy})\frac{\partial^2 w}{\partial x^2} + (\varepsilon_{yy} + \nu\varepsilon_{xx})\frac{\partial^2 w}{\partial y^2} + 2(1-\nu)\varepsilon_{xy}\frac{\partial^2 w}{\partial x \partial y}\right) \tag{4}$$

$$\frac{\partial}{\partial x}(\varepsilon_{xx} + \nu\varepsilon_{yy}) + (1-\nu)\frac{\partial \varepsilon_{xy}}{\partial y} = 0 \tag{5}$$

$$\frac{\partial}{\partial y}(\varepsilon_{yy} + \nu\varepsilon_{xx}) + (1-\nu)\frac{\partial \varepsilon_{xy}}{\partial x} = 0 \tag{6}$$

with density ρ, flexural stiffness $\mathcal{D} = Eh^3/(12(1-\nu^2))$, Poisson ratio ν, modulus of elasticity E, and applied external load g. Partial differentiation with respect to a given variable is denoted by a comma subscript proceeded by that variable. Substitution of Eqs. (1–3) into Eqs. (4–6) yields the familiar $w-u-v$ formulation [20]:

$$\rho h w_{,tt} + \mathcal{D}\nabla^4 w = g + \frac{12\mathcal{D}}{h^2}\left[\left(u_{,x} + \frac{1}{2}w_{,x}^2\right)(w_{,xx} + \nu w_{,yy}) + \left(v_{,y} + \frac{1}{2}w_{,y}^2\right)(w_{,yy} + \nu w_{,xx}) + (1-\nu)(u_{,y} + v_{,x} + w_{,x}w_{,y})w_{,xy}\right] \tag{7}$$

$$u_{,xx} + w_{,x}w_{,xx} + \left(\frac{1-\nu}{2}\right)(u_{,yy} + w_{,x}w_{,yy}) + \left(\frac{1+\nu}{2}\right)(v_{,xy} + w_{,y}w_{,xy}) = 0 \tag{8}$$

$$v_{,yy} + w_{,y}w_{,yy} + \left(\frac{1-\nu}{2}\right)(v_{,xx} + w_{,y}w_{,xx}) + \left(\frac{1+\nu}{2}\right)(u_{,xy} + w_{,x}w_{,xy}) = 0 \tag{9}$$

A. Model Reduction Using Quadratic Components

The approach of the method of quadratic components is to discretize the equations of motion such that the full nonlinear system retains only as many degrees of freedom as the number of bending modes retained. The resulting, discretized equations of motion require that only one nonlinear system of equations needs to be solved at each time step when solving for the temporal solution. By comparison, the traditional solution approach employed in aeroelastic calculations requires that the nonlinear membrane equations, coupled to the nonlinear bending equation, must be solved simultaneously. A further advantage of the method of quadratic components is that it allows for the nonlinear plate problem to be solved with far fewer degrees of freedom than the alternative approaches presented in the literature, because there will only be as many degrees of freedom as there are bending modes.

The method of quadratic components consists of the selection of a set of basis functions $\{\underline{\phi}_n\}$ appropriate for the linearized equations and postulating a solution to the nonlinear equation of the form

$$\underline{\mathcal{W}}(x, y, t) = \sum_n \alpha_n(t)\underline{\phi}_n(x, y) + \sum_{n,m\le n} \alpha_n(t)\alpha_m(t)\underline{G}_{nm}(x, y) \tag{10}$$

where the $\underline{G}_{nm}(x, y)$ are selected such that the expansion of (10) can solve a quasi-static version of the governing equation correctly to within second order in $\{\alpha_n\}$. The α_n are the same variable in both the linear and quadratic terms because of the coupling between in-plane and out-of-plane displacements. The full expansion is then substituted into the dynamic governing differential equations to achieve nonlinear equations for the $\{\alpha_n\}$. Usually, but not always, the $\{\underline{\phi}_n\}$ are selected to be the eigensolutions to the linearized equations. The method for solving for the $\underline{G}_{nm}(x)$ is illustrated in the following and is discussed at length in [21,22].

In the context of the von Kármán plate equations, the method of quadratic components begins by identifying the eigenmodes $\underline{\phi}_n$ and

natural frequencies Ω_n of the linearized homogeneous equation of motion:

$$\rho h w_{,tt} + \mathcal{D}\nabla^4 w = 0 \tag{11}$$

The eigenmodes of the linear plate $\underline{\phi}_n$ are then used to construct an orthogonal set of modal forces $\{f_n\}$. In the following discussion, however, the derivation does not necessitate this choice of basis. For the purpose of expanding the response $\underline{\mathcal{N}}$ of the nonlinear plate, the forces

$$\underline{f}(x,y) = \sum_{n=1}^{N} \alpha_i K \underline{\phi}_n(x,y) \tag{12}$$

are applied statically in an arbitrary linear combination to a finite element model of the nonlinear plate, where K is the stiffness of the linear plate. Next, the full kinematics of the plate are postulated as consisting of a linear component and a quadratic component, and the response $\underline{\mathcal{N}}$ is numerically calculated using the commercial finite element code ABAQUS in order to determine the linear and quadratic components of Eq. (10).

The Taylor series expansion for a multivariate expression centered about the origin is given as

$$\underline{\mathcal{N}}(\alpha_1,\alpha_2,\ldots,\alpha_N) = [\alpha_1 \quad \alpha_2 \quad \cdots \quad \alpha_N] \begin{bmatrix} \partial \underline{f}/\partial\alpha_1 \\ \partial \underline{f}/\partial\alpha_2 \\ \vdots \\ \partial \underline{f}/\partial\alpha_N \end{bmatrix} + \frac{1}{2}[\alpha_1 \quad \alpha_2 \quad \cdots \quad \alpha_N] \begin{bmatrix} \partial^2\underline{f}/\partial\alpha_1^2 & \partial^2\underline{f}/\partial\alpha_2\partial\alpha_1 & \cdots & \partial^2\underline{f}/\partial\alpha_N\partial\alpha_1 \\ \partial^2\underline{f}/\partial\alpha_1\partial\alpha_2 & \partial^2\underline{f}/\partial\alpha_2^2 & \cdots & \partial^2\underline{f}/\partial\alpha_N\partial\alpha_2 \\ \vdots & \vdots & \ddots & \vdots \\ \partial^2\underline{f}/\partial\alpha_1\partial\alpha_N & \partial^2\underline{f}/\partial\alpha_2\alpha_N & \cdots & \partial^2\underline{f}/\partial\alpha_N^2 \end{bmatrix} \begin{bmatrix} \alpha_1 \\ \alpha_2 \\ \vdots \\ \alpha_N \end{bmatrix} + \cdots \tag{13}$$

The response of the structure $\underline{\mathcal{W}}$ is thus written in terms of the Taylor series up through quadratic terms:

$$\underline{\mathcal{W}}(x,y,t) = \underline{\mathcal{N}}(\alpha_1,\alpha_2,\ldots,\alpha_N) = \sum_{n=1}^{N} \alpha_n \underline{Y}_n(x,y) + \sum_{n=1}^{N}\sum_{m=1}^{N} \frac{1}{2}\alpha_n\alpha_m \underline{G}_{nm}(x,y) \tag{14}$$

where

$$\underline{Y}_n(x,y) = \frac{\partial \underline{f}}{\partial \alpha_n} \tag{15}$$

and

$$\underline{G}_{nm}(x,y) = \frac{\partial^2 \underline{f}}{\partial\alpha_n\partial\alpha_m} \tag{16}$$

With this nomenclature, the unit normal vectors are denoted as $\underline{i}$, $\underline{j}$, and $\underline{k}$ in the x, y, and z directions, respectively. Note that the time dependence of Eq. (14) is in terms of the α_n.

The derivatives $\partial \underline{f}/\partial\alpha_i$ and $\partial^2 \underline{f}/\partial\alpha_i\partial\alpha_j$ are calculated via finite difference approximations. In what follows, third- and fifth-order finite difference expressions are used; however, higher-order expressions may be used. For each quantity, two low-order finite difference approximations are constructed and are then used to compose the higher-order approximation:

$$\underline{Y}_n^{(a)} = \frac{\underline{\mathcal{N}}(\alpha_n) - \underline{\mathcal{N}}(-\alpha_n)}{2\alpha_n} \tag{17}$$

$$\underline{Y}_n^{(b)} = \frac{\underline{\mathcal{N}}(2\alpha_n) - \underline{\mathcal{N}}(-2\alpha_n)}{4\alpha_n} \tag{18}$$

$$\underline{Y}_n = (4/3)\underline{Y}_n^{(a)} - (1/3)\underline{Y}_n^{(b)} \tag{19}$$

$$\underline{G}_{nn}^{(a)} = \frac{\underline{\mathcal{N}}(\alpha_n) + \underline{\mathcal{N}}(-\alpha_n)}{\alpha_n^2} \tag{20}$$

$$\underline{G}_{nn}^{(b)} = \frac{\underline{\mathcal{N}}(2\alpha_n) + \underline{\mathcal{N}}(-2\alpha_n)}{4\alpha_n^2} \tag{21}$$

$$\underline{G}_{nn} = (4/3)\underline{G}_{nn}^{(a)} - (1/3)\underline{G}_{nn}^{(b)} \tag{22}$$

$$\underline{G}_{nm}^{(a)} = \frac{\underline{\mathcal{N}}(\alpha_n,\alpha_m) + \underline{\mathcal{N}}(-\alpha_n,-\alpha_m) - \underline{\mathcal{N}}(\alpha_n,-\alpha_m) - \underline{\mathcal{N}}(-\alpha_n,\alpha_m)}{4\alpha_n\alpha_m} \tag{23}$$

$$\underline{G}_{nm}^{(b)} = \frac{\underline{\mathcal{N}}(2\alpha_n,2\alpha_m) + \underline{\mathcal{N}}(-2\alpha_n,-2\alpha_m) - \underline{\mathcal{N}}(2\alpha_n,-2\alpha_m) - \underline{\mathcal{N}}(-2\alpha_n,2\alpha_m)}{16\alpha_n\alpha_m} \tag{24}$$

$$\underline{G}_{nm} = (4/3)\underline{G}_{nm}^{(a)} - (1/3)\underline{G}_{nm}^{(b)} \tag{25}$$

The notations $\underline{\mathcal{N}}(\alpha_n)$ and $\underline{\mathcal{N}}(\alpha_n,\alpha_m)$ are meant to indicate that the only nonzero elements of $[\alpha_1,\alpha_2,\ldots,\alpha_N]$ are α_n, and α_n and α_m, respectively. Because $\underline{Y}$ is the linear component of the expansion, a converged solution for the coefficients yields that $\underline{Y}_n = c\underline{\phi}_n^{(k)}(x,y)$ when $\underline{\phi}_n^{(k)}$ is resolved in the $\underline{k}$ direction, and c is a constant based on the normalization method. In practice, the values for α are reduced until the coefficients have converged. As the basis functions are computed from these numerical derivatives, higher-order approximations will yield more accurate results.

The large deformation theory of plates manifests a lateral stiffening due to the membrane stretching, which is captured by a quadratic coupling in the kinematics. This is a second order coupling between the membrane strain and the lateral displacements [19,23,24]. The out-of-plane and in-plane displacements are thus expressed as

$$w(x,y,t) = \sum_{n=1}^{N} \alpha_n(t) W^{(n)}(x,y) = \sum_{n=1}^{N} \alpha_n \underline{Y}_n(x,y) \tag{26}$$

$$u(x,y,t) = \sum_{n=1}^{N}\sum_{m=1}^{n} \alpha_n(t)\alpha_m(t) U^{(nm)}(x,y) \tag{27}$$

$$v(x,y,t)=\sum_{n=1}^{N}\sum_{m=1}^{n}\alpha_n(t)\alpha_m(t)V^{(nm)}(x,y) \tag{28}$$

with $U^{(nm)}$ and $V^{(nm)}$ being the components of $\underline{G}_{nm}$ taken in the $\underline{i}$ and $\underline{j}$ directions, respectively. Substitution of Eqs. (26–28) into Eqs. (8) and (9) and matching coefficients yields that for each $\alpha_n\alpha_m$,

$$\begin{aligned}&2U^{(mn)}_{,xx}+(1+\nu)V^{(mn)}_{,xy}+(1-\nu)U^{(mn)}_{,yy}\\&\quad=-2(W^{(m)}_{,x}W^{(n)}_{,xx}+W^{(n)}_{,x}W^{(m)}_{,xx})-(1+\nu)(W^{(m)}_{,y}W^{(n)}_{,xy}\\&\quad+W^{(n)}_{,y}W^{(m)}_{,xy})-(1-\nu)(W^{(m)}_{,x}W^{(n)}_{,yy}+W^{(n)}_{,x}W^{(m)}_{,yy})\end{aligned} \tag{29}$$

and

$$\begin{aligned}&2V^{(mn)}_{,yy}+(1+\nu)U^{(mn)}_{,xy}+(1-\nu)V^{(mn)}_{,xx}\\&\quad=-2(W^{(m)}_{,y}W^{(n)}_{,yy}+W^{(n)}_{,y}W^{(m)}_{,yy})-(1+\nu)(W^{(m)}_{,x}W^{(n)}_{,xy}\\&\quad+W^{(n)}_{,x}W^{(m)}_{,xy})-(1-\nu)(W^{(m)}_{,y}W^{(n)}_{,xx}+W^{(n)}_{,y}W^{(m)}_{,xx})\end{aligned} \tag{30}$$

Equations (29) and (30) are for the quasi-static in-plane displacement when the right hand sides are taken as distributed body forces in the $\underline{i}$ and $\underline{j}$ directions, respectively. For any m, n, and appropriate in-plane boundary conditions, it is possible to solve for $U^{(mn)}$ and $V^{(mn)}$ in terms of $W^{(m)}$, $W^{(n)}$, and their derivatives.

B. Galerkin Formulation

With $U^{(mn)}$ and $V^{(mn)}$ known in terms of $W^{(m)}$, $W^{(n)}$, and their derivatives, substitution of Eqs. (26–28) into Eq. (7) yields the N equations of motion in terms of α (with $s\in[1,2,\ldots,N]$):

$$\begin{aligned}&\alpha_{s,tt}\rho hW^{(s)}+\alpha_s\mathcal{D}\nabla^4W^{(s)}\\&-\frac{12\mathcal{D}}{h^2}\sum_{r=1}^{N}\sum_{n=1}^{N}\sum_{m=1}^{N}\Bigg[\left(\alpha_n\alpha_mU^{(nm)}_{,x}+\frac{1}{2}\alpha_nW^{(n)}_{,x}\alpha_mW^{(m)}_{,x}\right)(\alpha_rW^{(r)}_{,xx}\\&+\alpha_r\nu W^{(r)}_{,yy})+\left(\alpha_n\alpha_mV^{(nm)}_{,y}+\frac{1}{2}\alpha_nW^{(n)}_{,y}\alpha_mW^{(m)}_{,y}\right)(\alpha_rW^{(r)}_{,yy}\\&+\alpha_r\nu W^{(r)}_{,xx})+(1-\nu)(\alpha_n\alpha_mU^{(nm)}_{,y}+\alpha_n\alpha_mV^{(nm)}_{,x}\\&+\alpha_nW^{(n)}_{,x}\alpha_mW^{(m)}_{,y})\alpha_rW^{(r)}_{,xy}\Bigg]=g\end{aligned} \tag{31}$$

Contracting both sides with $W^{(s)}$ yields the Galerkin formulation, which is cubic in α. Because $W^{(s)}$ is proportional to the sth eigenvector of the linearized problem,

$$\alpha_{s,tt}+\omega_s^2\alpha_s+\sum_{r=1}^{N}\sum_{n=1}^{N}\sum_{m=1}^{N}P_{srnm}\alpha_r\alpha_n\alpha_m=G_s(t) \tag{32}$$

where

$$\omega_s^2=\int_0^{L_x}\int_0^{L_y}W^{(s)}\mathcal{D}\nabla^4W^{(s)}\,\mathrm{d}y\,\mathrm{d}x \tag{33}$$

$$G_s(t)=\int_0^{L_x}\int_0^{L_y}W^{(s)}g\,\mathrm{d}y\,\mathrm{d}x \tag{34}$$

and

$$\begin{aligned}P_{srnm}=-\frac{12\mathcal{D}}{h^2}\int_0^{L_x}\int_0^{L_y}W^{(s)}\Bigg[&\left(U^{(nm)}_{,x}+\frac{1}{2}W^{(n)}_{,x}W^{(m)}_{,x}\right)(W^{(r)}_{,xx}\\&+\nu W^{(r)}_{,yy})+\left(V^{(nm)}_{,y}+\frac{1}{2}W^{(n)}_{,y}W^{(m)}_{,y}\right)(W^{(r)}_{,yy}+\nu W^{(r)}_{,xx})\\&+(1-\nu)(U^{(nm)}_{,y}+V^{(nm)}_{,x}+W^{(n)}_{,x}W^{(m)}_{,y})W^{(r)}_{,xy}\Bigg]\mathrm{d}y\,\mathrm{d}x\end{aligned} \tag{35}$$

In practice, only half of the elements of P need to be calculated as $P_{srnm}=P_{srmn}$. The corresponding matrix form of Eq. (32) is written as

$$\mathbb{I}\underline{\alpha}_{,tt}+\mathrm{diag}(\omega_s^2)\underline{\alpha}+\begin{bmatrix}\underline{\alpha}^T\mathbb{P}_{11}\underline{\alpha} & \cdots & \underline{\alpha}^T\mathbb{P}_{1N}\underline{\alpha}\\ \vdots & \ddots & \vdots\\ \underline{\alpha}^T\mathbb{P}_{N1}\underline{\alpha} & \cdots & \underline{\alpha}^T\mathbb{P}_{NN}\underline{\alpha}\end{bmatrix}\underline{\alpha}=\underline{G}(t) \tag{36}$$

Here, $\mathbb{I}$ denotes the identity matrix, $\mathrm{diag}(\omega_s^2)$ indicates a diagonal matrix with nonzero values corresponding to the squares of the natural frequencies in order of $s=1$ to N, and

$$\mathbb{P}_{ab}=\begin{bmatrix}P_{ab11} & \cdots & P_{ab1N}\\ \vdots & \ddots & \vdots\\ P_{abN1} & \cdots & P_{abNN}\end{bmatrix} \tag{37}$$

The advantage of this system of coupled, nonlinear differential equations is that there are only as many degrees of freedom as there are bending modes. Additionally, no further spatial integrations must be performed once the coefficients and $\underline{G}(t)$ are calculated.

C. Implicit Time Integration Method

Solutions of the nonlinear equation (32) for α are available through power series methods, harmonic balance/Fourier series methods, and other approximate solutions. However, in order to efficiently account for an arbitrary applied pressure g, an implicit integration method, the Hilber–Hughes–Taylor (HHT) method [25,26], is applied. Because of the nonlinearities of Eq. (32), the first step in the solution is to guess a solution at the next time step $\underline{\chi}=\underline{\alpha}(t_{n+1})$. The mass and stiffness matrices for the system are then defined as

$$\mathbb{M}=\mathbb{I} \tag{38}$$

and

$$\mathbb{K}(\underline{\chi})=\mathrm{diag}(\omega_s^2)+\begin{bmatrix}\underline{\chi}^T\mathbb{P}_{11}\underline{\chi} & \cdots & \underline{\chi}^T\mathbb{P}_{1N}\underline{\chi}\\ \vdots & \ddots & \vdots\\ \underline{\chi}^T\mathbb{P}_{N1}\underline{\chi} & \cdots & \underline{\chi}^T\mathbb{P}_{NN}\underline{\chi}\end{bmatrix} \tag{39}$$

From the HHT method, with modal acceleration $\underline{\xi}$ and modal velocity $\underline{\zeta}$,

$$\mathbb{M}\underline{\xi}(t_{n+1})+(1+\lambda)\mathbb{K}(\underline{\chi})\underline{\alpha}(t_{n+1})-\lambda\mathbb{K}(\underline{\chi})\underline{\alpha}(t_n)=\underline{G}(t_{n+1+\lambda}) \tag{40}$$

where

$$\underline{\alpha}(t_{n+1})=\underline{\alpha}(t_n)+\Delta t\underline{\zeta}(t_n)+\frac{\Delta t^2}{2}[(1-2\beta)\underline{\xi}(t_n)+2\beta\underline{\xi}(t_{n+1})] \tag{41}$$

$$\underline{\zeta}(t_{n+1})=\underline{\zeta}(t_n)+\Delta t[(1-\gamma)\underline{\xi}(t_n)+\gamma\underline{\xi}(t_{n+1})] \tag{42}$$

$$\begin{aligned}\underline{\xi}(t_{n+1})=[\mathbb{M}+(1+\lambda)\Delta t^2\beta\mathbb{K}(\underline{\chi})]^{-1}\Bigg[&\underline{G}(t_{n+1+\lambda})\\&-\left((1+\lambda)\frac{\Delta t^2}{2}(1-2\beta)\mathbb{K}(\underline{\chi})\right)\underline{\xi}(t_n)\\&-((1+\lambda)\Delta t\mathbb{K}(\underline{\chi}))\underline{\zeta}(t_n)-\mathbb{K}(\underline{\chi})\underline{\alpha}(t_n)\Bigg]\end{aligned} \tag{43}$$

$$t_{n+1+\lambda}=t_{n+1}+\lambda\Delta t \tag{44}$$

$$\beta=\frac{1-\lambda^2}{4} \tag{45}$$

and

$$\gamma=\frac{1-2\lambda}{2} \tag{46}$$

In practice, Eq. (43) is solved via lower/upper (LU) decomposition, and a typical value for $\lambda = -0.05$. Next, the residual $R = \underline{\alpha}(t_{n+1}) - \underline{\chi}$ is calculated, and the procedure is repeated with a new guess for $\underline{\chi}$ until $R \to 0$.

D. Static Pressure Validation Example

In Fig. 1, a plate with simply supported conditions at $x = 0$ and $x = L_x$ and free boundary conditions at $y = 0$ and $y = L_y$ is modeled. The material properties are based on aluminum and are listed in Table 1 along with the geometric properties. Four different solutions for the displacement of this plate are considered: an explicit closed-form solution for the linear plate [27], a one-term approximation for the nonlinear plate, the numerical results calculated using the ABAQUS software package for the nonlinear plate, and the nonlinear model discretized in the previous sections using five mode shapes (i.e., $N = 5$). The applied pressure in all cases is a constant uniform pressure with magnitude F.

1. *One-Term Approximation*

The one-term approximation is developed with the assumption that the displacement does not vary in y. In this case, the problem is reduced to that of a beam. The eigenmodes for this problem are

$$W^{(n)}(x) = c_0 \sin\frac{n\pi x}{L_x} \tag{47}$$

where

$$c_0 = \sqrt{\frac{2}{L_x \rho h L_y}}$$

Taking only the first mode, the equation for the lateral deformation $U^{(11)}$ is

$$U^{(11)}_{,xx} = -W^{(1)}_{,x} W^{(1)}_{,xx} \tag{48}$$

Substitution into Eq. (47) yields the in-plane displacement

$$U^{(11)} = -\frac{c_0^2 \pi}{8L_x} \sin\left(\frac{2\pi x}{L_x}\right) \tag{49}$$

With a lateral deflection of $w(x) = \alpha W^{(1)}(x)$, the longitudinal strain due to the lateral deformation and the strain of the corresponding longitudinal displacement are

$$\epsilon_w = \frac{1}{2} w^2_{,x} = \frac{\alpha^2 \pi^2}{L_x^4 \rho h} \cos^2\left(\frac{\pi x}{L_x}\right) \tag{50}$$

$$\epsilon_u = \alpha^2 \frac{\partial U^{11}}{\partial x} = -\alpha^2 \frac{\pi^2}{2L_x^4 \rho h} \cos^2\left(\frac{2\pi x}{L_x}\right) \tag{51}$$

Combining these two strain components and substituting into the governing equation yields the one-term approximation for α:

$$\alpha_{,tt} + \omega^2 \alpha + \alpha^3 \left[\left(\frac{12\mathcal{D}}{h^2}\right)\left(\frac{\pi^4}{2L_x^5}\right)\left(\frac{1}{\rho h L_x}\right)^3\right] = \int_0^{L_x} g(x) W^{(1)}\, \mathrm{d}x \tag{52}$$

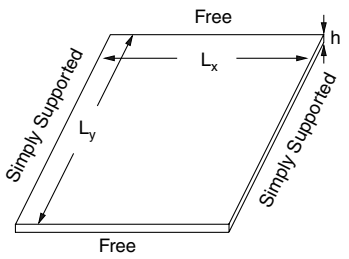

Fig. 1 Geometry of the problem considered in the example.

Table 1 System parameters for the comparison with [13]

Variable	Value
Plate modulus of elasticity E	75.378 GPa
Plate thickness h	4.6 mm
Plate length in the downstream direction L_x	1 m
Plate length in the cross-stream direction L_y	1 m
Plate density ρ	2770 kg/m^3
Poisson's ratio of the plate ν	0.33
Mach number M	2

For the present quasi-static problem, solution of Eq. (52) reduces to determining the roots of a polynomial as $g(x) = F$ is a constant.

2. *Results*

The results for the four solution methods are shown in Fig. 2 on a logarithmic plot and Fig. 3 on a linear plot. For pressures below $F = 100$, all four solutions show good agreement. Above $F = 100$, the linear solution diverges from the three nonlinear solutions. While the one-term approximation exhibits the stiffening behavior associated with the von Kármán plate equations, there is a 30% relative error, with respect to the numerical solution, in the maximum deflection of the plate for $F = 1000$, and for the discretization method presented in the previous sections with $N \geq 3$, a 5.0% relative error is observed with respect to the numerical solution. Additionally, the present method is found to yield converged results with only $N = 3$ modes.

In terms of computational efficiency, the linear and one-term solutions were both completed in under 1 s. The numerical solution in ABAQUS with three modes and 2500 elements (a 50×50 grid), the minimum needed for a fully converged solution due to the nonlinear nature of the problem, required 27.5 min for the entire loading branch (which included 61 load levels), while the present method with five modes took 2.65 min using a simplex algorithm [28] to efficiently minimize the residuals R once the coefficients $\underline{G}_{nm}$ and $\underline{Y}_n$ had been calculated (this is equivalent to 2.6 s per load step, including pre- and postprocessing, where most of the computational time is spent). All simulations were calculated using a single processor.

III. Fluid–Structure Interaction

With the matrix form of the equation of motion now specified in terms of one variable in Eq. (36), the fluid model can be introduced via the forcing function $\underline{G}(t)$. The linearized quasi-steady pressure relationship of piston theory for a flow with speed Υ, density ρ_f, and Mach number M is given as [13]

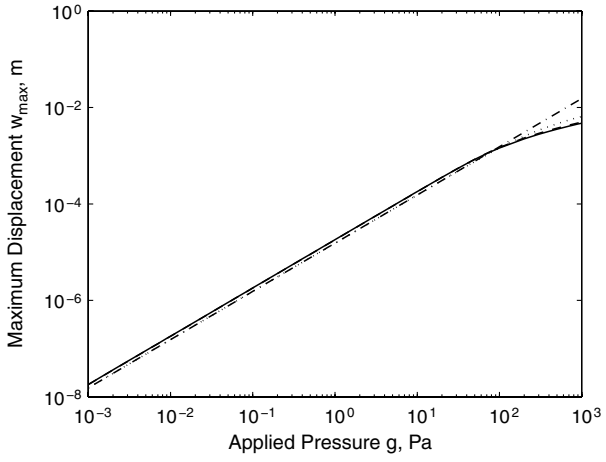

Fig. 2 Log plot of the four solutions to the quasi-static example: the present method (solid line), numerical results from ABAQUS (dashed line), the one-term approximation (dotted line), and the explicit linear solution [27] (dashed–dotted line).

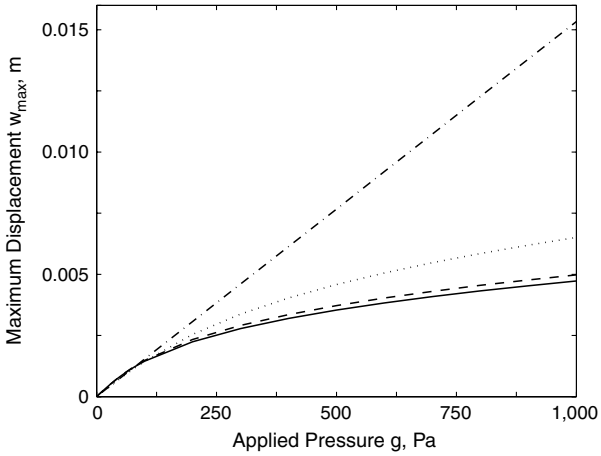

Fig. 3 Linear plot of the four solutions to the quasi-static example; the present method (solid line), numerical results from ABAQUS (dashed line), the one-term approximation (dotted line), and the explicit linear solution [27] (dashed–dotted line).

$$p - p_\infty = w_{,t}\frac{\rho_f \Upsilon}{\rho h}\frac{M^2-2}{(M^2-1)^{3/2}} + w_{,x}\frac{\rho_f \Upsilon^2}{(M^2-1)^{1/2}} \tag{53}$$

In terms of the Galerkin formulation (32), the applied force becomes

$$G_s = -\int W^{(s)}(p-p_\infty)\,\mathrm{d}A = -\zeta_s\frac{\rho_f\Upsilon}{\rho h}\frac{M^2-2}{(M^2-1)^{3/2}} - \frac{\rho_f\Upsilon^2}{(M^2-1)^{1/2}}\sum_{n=1}^{N}\alpha_n\int W^{(s)}W^{(n)}_{,x}\,\mathrm{d}A \tag{54}$$

To find the amplitudes and periods of the limit cycles excited by the fluid flow over the plate, a cyclic method similar to [29,30] is employed, which is similar to numerical continuation [31]. In this method, the modal amplitudes α_n and period of vibration for the system T are sought such that

$$\alpha_n(t) = \alpha_n(t+T) \qquad \zeta_n(t) = \zeta_n(t+T) \qquad \xi_n(t) = \xi_n(t+T) \tag{55}$$

The period T is found by simulating the response over a time long enough to include several periods, then choosing the T that minimizes the residuals of Eq. (55). For cases that do not converge after one simulation, a simplex algorithm is employed to minimize both T and α_n, ζ_n, and ξ_n efficiently. Once T is found, the modal periods are found by calculating the number of periods for each mode per period of the system. In practice, once α_n, ζ_n, ξ_n, and T are found for one value of a parameter being varied, either by a transient analysis or minimization algorithm, the α_n, ζ_n, ξ_n, and T are quickly found for an adjacent value of the parameter being studied by using the previous value's results as an initial guess for the next value.

A. Comparison to Classical Results

For the present analysis, the Mach number is held constant, while the speed of sound in the fluid μ is varied, with the fluid speed

$$\Upsilon = \mu M \tag{56}$$

and fluid density

$$\rho_f = \frac{\rho h M}{10} \tag{57}$$

This allows for the direct comparison to the results of Dowell [13] and more recent studies [16–18]. The relationship between Dowell's nondimensionalized nomenclature and the variables in the present analysis are given for the dynamic pressure and period, respectively:

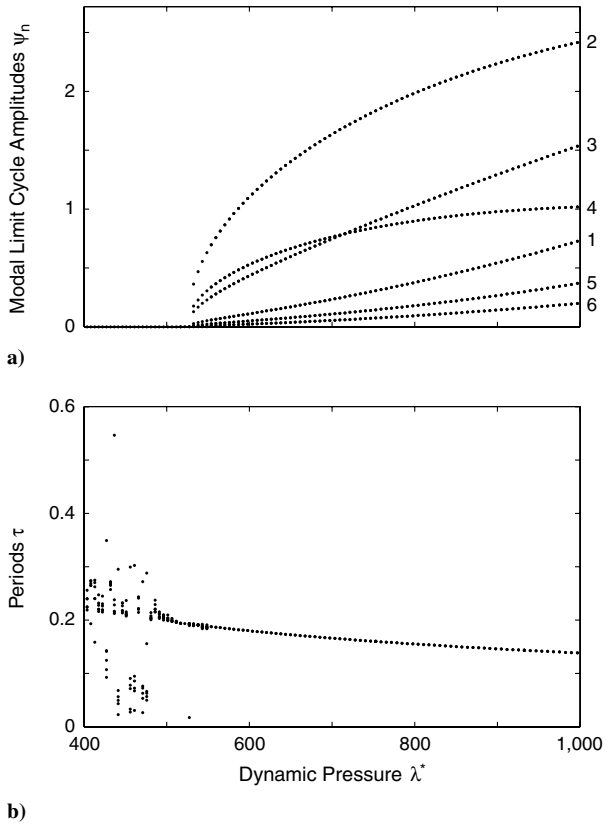

Fig. 4 Limit cycle a) amplitudes and b) periods for each mode included in the analysis as a function of the nondimensional dynamic pressure. Mode numbers are indicated on the right side of the figure.

$$\lambda^* = \frac{3\rho_f\Upsilon^2 L_x^3}{2\mathcal{D}\sqrt{M^2-1}} \tag{58}$$

$$\tau = T\sqrt{\frac{\mathcal{D}}{\rho h L_x^4}} \tag{59}$$

The plate is modeled with the material properties of aluminum and geometrical properties listed in Table 1. In keeping with the analysis of [13], the first six mode shapes that have no variation in y are used in what follows. Defining the quantities

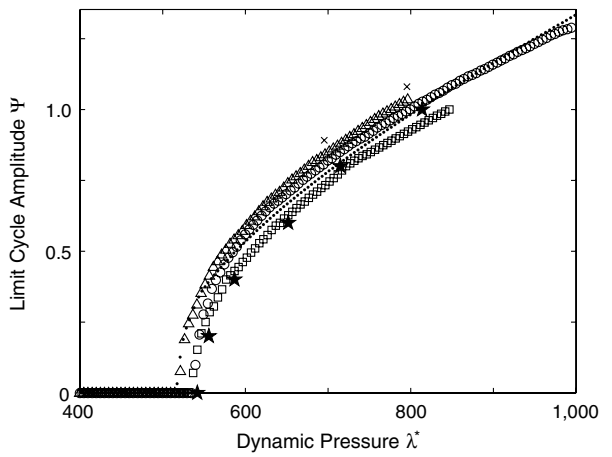

Fig. 5 Limit cycle amplitudes for the total plate response at $x = 0.75L_x$ and $y = 0.5L_y$ as a function of the nondimensional dynamic pressure for the present work (●), [13] (○), [18] (★), [16] using rectangular (□) and triangular (△) elements, and [17] (×).

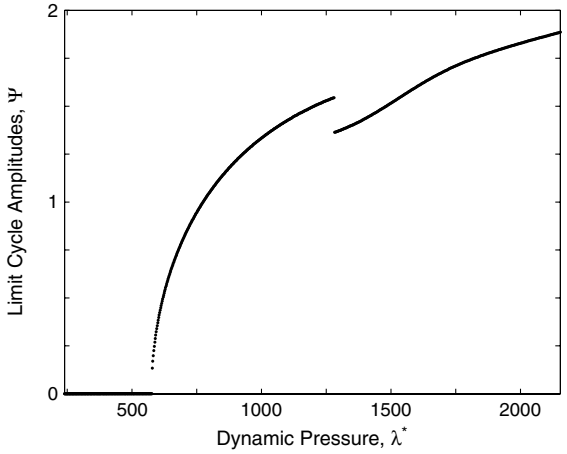

Fig. 6 Limit cycle amplitudes for the total plate response at $x = 0.75L_x$ and $y = 0.5L_y$ as a function of the nondimensional dynamic pressure.

$$\psi_n = \max \frac{\alpha_n(t) W^{(n)}(x, y)}{h} \quad \forall\ x \in [0, L_x], \quad \forall\ y \in [0, L_y], \quad \forall\ t \tag{60}$$

$$\Psi = \max \frac{w(\frac{3}{4}L_x, \frac{1}{2}L_y, t)}{h} \quad \forall\ t \tag{61}$$

the modal limit cycle amplitudes ψ_n and periods τ are calculated as a function of λ^* and are shown in Fig. 4. Below the onset of flutter, the τ do not converge to any particular limit cycle period as the modal amplitudes are approximately zero. Above the onset of flutter, though, the τ are convergent to the same value for all modes at a given λ^* as the plate undergoes forced vibration. The mode number for each modal limit cycle amplitude is indicated on the right side of Fig. 4a. While the modal coefficient for the first mode α_1 is higher than the other five modes, the product $\alpha_j W^{(j)}$ is greater for modes 2 through 4.

The onset of flutter for the primary limit cycle occurs at $\lambda^* = 525$. Between $\lambda^* = 480$ and the onset of the primary limit cycle, a second (nonzero) limit cycle was observed with an amplitude that is 8 orders of magnitude below the limit cycle amplitudes reported here. The present analysis is compared to the results of [13] in Fig. 5. The onset of flutter predicted by [13] occurs 4% higher (at $\lambda^* \approx 545$) than in the present method. Overall there is good agreement between the two models, though there is some discrepancy at lower values of λ^*.

The more recent analyses [16–18] of the same system are also compared to the results of the model developed in this paper and [13] in Fig. 5. Each of these analyses uses a finite element method; [16], in particular, studies two types of elements, a rectangular element and a higher-order discrete Kirchhoff theory triangular element, and also takes into account thermal effects. While the simulation results using the rectangular element have higher agreement with [13] near the onset of flutter, the triangular element is shown to have higher agreement than the rectangular element for $\lambda^* \geq 600$. A triangular element with the same number of degrees of freedom is also employed in the finite element analysis performed in [18], but the

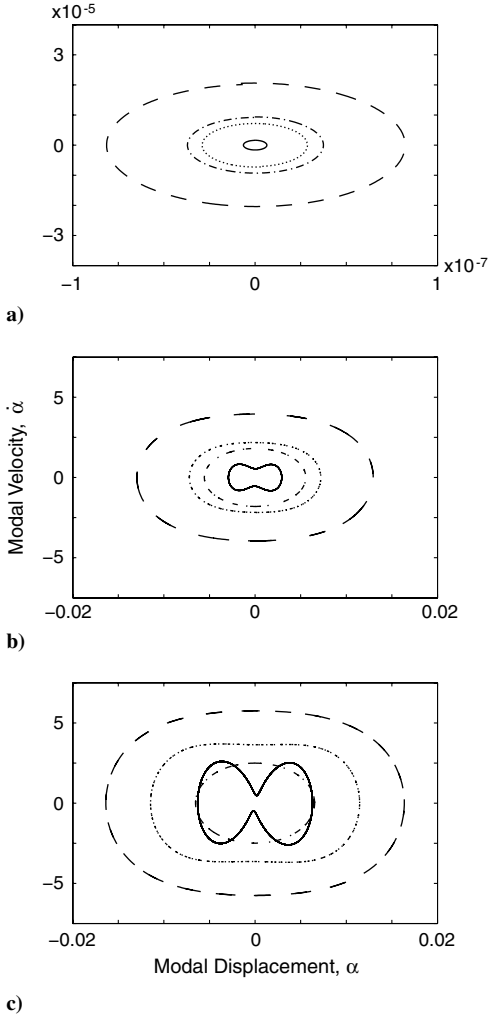

Fig. 7 Modal phase portraits for a) $\lambda^* = 575$, b) $\lambda^* = 957$, and c) $\lambda^* = 1280$; shown are modes 1 (dashed–dotted line), 2 (dashed line), 3 (dotted line), and 4 (solid line).

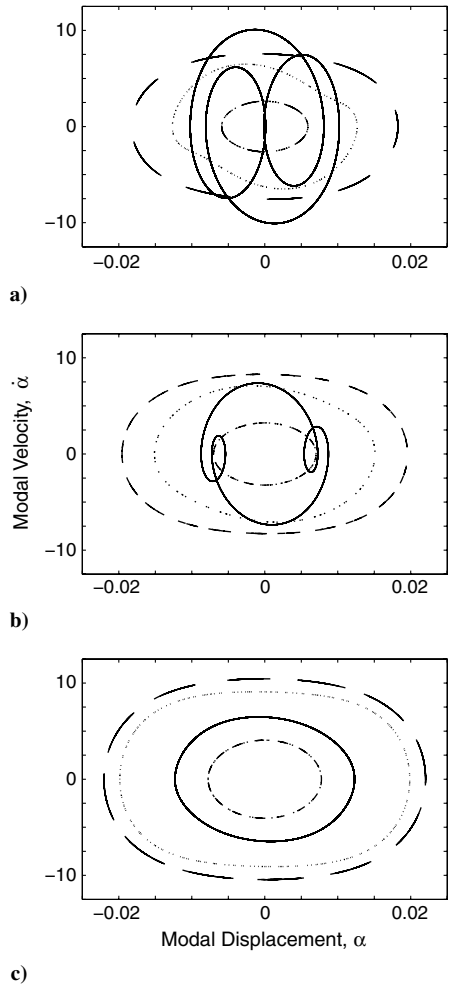

Fig. 8 Modal phase portraits for a) $\lambda^* = 1370$, b) $\lambda^* = 1650$, and c) $\lambda^* = 2150$; shown are modes 1 (dashed–dotted line), 2 (dashed line), 3 (dotted line), and 4 (solid line).

predicted limit cycle amplitudes with this element are appreciably below those predicted in [16]. The finite element analysis of [17] uses a rectangular four-node Bogner–Fox–Schmidt C^1 conforming element. The relative difference between [13,17] is greater than any of the other studies reported, but the modeling of [17] also takes into account acoustical and thermal loading. By contrast, the present analysis develops a reduced-order model that incorporates higher-order effects for the entire plate, which is a much more computationally efficient approach (in terms of degrees of freedom required) than what is reported in the literature, and it does not sacrifice accuracy.

For all results shown in Fig. 5, the disagreement is highest at the onset of flutter, but the results tend to converge to those of the present model away from onset. The analysis of [18], in particular, is shown to converge to the same limit cycle amplitude as λ^* increases, and the most recent study [17] is shown to be consistently higher than all other reported results. Possible variance between [13] and the present method includes [13] reporting values that had converged to within 5% of the $N \to \infty$ solution, which could account for all of the variance for $\lambda > 560$. Second, and to a lesser extent than the previous explanation, the values from [13,16–18] were interpolated from plots using electronic copies of the original papers. Overall, though, there is reasonable agreement between the methods.

B. Discontinuity in the Limit Cycle Amplitudes

In the previous studies [13,16–18], no results for dynamic pressures above $\lambda^* = 1200$ are reported for this set of parameters. In Fig. 6, the limit cycle amplitudes are calculated for dynamic pressures up to $\lambda^* = 2200$. At $\lambda^* = 1281$, a discontinuity is observed in the limit cycle amplitude. This discontinuity is attributable to a snap-through transition of the fourth mode, as seen in the phase portraits in Figs. 7 and 8. As λ^* increases to 1281, the phase portrait of the fourth mode develops two distinct lobes (Fig. 7c). At $\lambda^* = 1281$, the section between the two lobes coincides for both the upper and lower halves of the phase portrait. As a result, subsequent phase portraits show that the motion has transitioned to an entirely new shape (Fig. 8a). Coupling between the modes results in the ovular shape of the phase portraits for modes one through three becoming more oblique. This is especially prominent for the third mode.

As λ^* is further increased, the phase portraits for all modes gradually return to an ovular shape. The phases of these mode shapes, relative to the first mode, are shown in Fig. 9. Between the onset of flutter and $\lambda^* = 1281$, the phases of the limit cycles are shown to be steady; however, at the critical value $\lambda^* = 1281$, the phases of modes two through four are shown to change 180° with respect to the first mode's phase. Above $\lambda^* = 1281$, the phases transition back to their values before the discontinuity in order of mode number, which corresponds to the rate at which the phase portraits for each mode transitions back to an ovular shape (Fig. 7). Note that if the limit cycle amplitude curve below $\lambda^* = 1281$ in Fig. 6 is projected out to $\lambda^* = 2200$, it represents an asymptote that the limit cycle amplitudes above $\lambda^* = 1281$ approach.

This new set of coexisting limit cycle phase portraits that give rise to the discontinuity in the limit cycle amplitude has not been previously reported. Because of the reduced limit cycle amplitude above $\lambda^* = 1281$, the results indicate that when operation in high-limit-cycle-amplitude regimes is unavoidable, the limit cycle amplitude may be able to be attenuated by increasing a system parameter such that a higher limit cycle regime is engaged. Because the limit cycles on either side of $\lambda^* = 1281$ have their own unique character, it suggests that these limit cycles could be used as bases for the nonlinear analysis of similar problems.

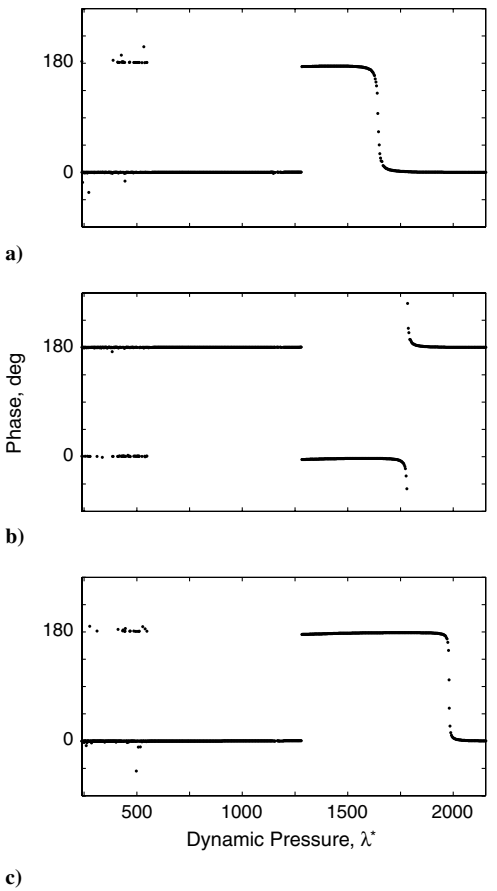

Fig. 9 Phase as a function of the nondimensional dynamic pressure relative to the first mode for the a) second mode, b) third mode, and c) fourth mode.

IV. Conclusions

A reduced-order model for von Kármán plates is developed in this paper and discretized in both space by a Galerkin approximation and time with an implicit integration scheme. The model developed here is both more computationally efficient (with respect to degrees of freedom required) and as accurate as the other models described in the literature. The reduced-order model of the von Kármán plate is subsequently validated using a numerical analysis for the case of a static plate, and by comparison to the classic results of [13] for the case of a plate under quasi-steady pressure fluid flow. In the sequel to this paper, the model will be further extended to the case of a full fluid flow. The primary results and contributions of this paper are as follows:

1) The full kinematics of a von Kármán plate can be postulated as consisting of both linear and quadratic components. These are found by first identifying the eigenmodes and natural frequencies of the linear plate, then using them in a multivariate expansion to find the response of the nonlinear plate.

2) The advantage of the method developed is that it requires only as many degrees of freedom as there are bending modes, which is far fewer degrees of freedom than other methods in the literature, making it a more practical approach to studying problems involving nonlinear plates.

3) The method is validated for a plate with a uniform load using both numerical and classical results, and it is shown that the computational time required for it is significantly less than that of other numerical methods.

4) The application of the model developed in this paper to the problem of quasi-steady fluid flow shows that the predicted results are in good agreement with results previously reported in [13,16–18].

5) A critical nondimensional dynamic pressure is shown to exist, at which a snap-through occurs in the shape of the phase portraits. This yields a discontinuity in the limit cycle amplitudes that has not been previously investigated.

Acknowledgments

Sandia National Laboratories is a multiprogram laboratory operated by Sandia Corporation, a Lockheed Martin Company, for the U.S. Department of Energy's National Nuclear Security

Administration under contract DE-AC04-94-AL85000. The authors gratefully acknowledge the support of their colleagues, especially Matthew Barone.

References

[1] Milman, M. H., and Chu, C.-C., "Optimization Methods for Passive Damper Placement and Tuning," *Journal of Guidance, Control, and Dynamics*, Vol. 17, 1994, pp. 848–856. doi:10.2514/3.21275

[2] Castanier, M. P., Tan, Y.-C., and Pierre, C., "Characteristic Constraint Modes for Component Mode Synthesis," *AIAA Journal*, Vol. 39, 2001, pp. 1182–1187. doi:10.2514/2.1433

[3] Tan, Y.-C., Castanier, M. P., and Pierre, C., "Power Flow Analysis of Complex Structures Using Characteristic Constraint Modes," *AIAA Journal*, Vol. 43, 2005, pp. 1360–1370. doi:10.2514/1.14450

[4] Segalman, D. J., "Model Reduction of Systems with Localized Nonlinearities," *Journal of Computational and Nonlinear Dynamics*, Vol. 2, 2007, pp. 249–266. doi:10.1115/1.2727495

[5] Hung, E. S., and Senturia, S. D., "Generating Efficient Dynamical Models for Microelectromechanical Systems from a Few Finite-Element Simulation Runs," *Journal of Microelectromechanical Systems*, Vol. 8, 1999, pp. 280–289. doi:10.1109/84.788632

[6] Ribeiro, P., and Petyt, M., "Nonlinear Vibration of Plates by the Hierarchical Finite Element and Continuation Methods," *International Journal of Mechanical Sciences*, Vol. 41, 1999, pp. 437–459. doi:10.1016/S0020-7403(98)00076-9

[7] Zhao, X., Abdel-Rahman, E. M., and Nayfeh, A. H., "A Reduced-Order Model for Electrically Actuated Microplates," *Journal of Micromechanics and Microengineering*, Vol. 14, 2004, pp. 900–906. doi:10.1088/0960-1317/14/7/009

[8] Lim, H. S., and Yoo, H. H., "Modal Analysis of Cantilever Plates Undergoing Accelerated In-Plane Motion," *Journal of Sound and Vibration*, Vol. 297, 2006, pp. 880–894. doi:10.1016/j.jsv.2006.05.004

[9] Moussaoui, F., and Benamar, R., "Non-Linear Vibrations of Shell-Type Structures: A Review with Bibliography," *Journal of Sound and Vibration*, Vol. 255, 2002, pp. 161–184. doi:10.1006/jsvi.2001.4146

[10] Sheikh, A. H., and Hukhopadhyay, M., "Large Amplitude Free Flexural Vibration of Stiffened Plates," *AIAA Journal*, Vol. 34, 1996, pp. 2377–2383. doi:10.2514/3.13404

[11] Touzé, C., Thomas, O., and Chaigne, A., "Hardening/Softening Behaviour in Non-Linear Oscillations of Structural Systems Using Non-Linear Normal Modes," *Journal of Sound and Vibration*, Vol. 273, 2004, pp. 77–101. doi:10.1016/j.jsv.2003.04.005

[12] Luo, A. C. J., "An Approximate Theory for Geometrically Nonlinear Thin Plates," *International Journal of Solids and Structures*, Vol. 37, 2000, pp. 7655–7670. doi:10.1016/S0020-7683(99)00303-0

[13] Dowell, E. H., "Nonlinear Oscillations of a Fluttering Plate," *AIAA Journal*, Vol. 4, 1966, pp. 1267–1275. doi:10.2514/3.3658

[14] Mortara, S. A., Slater, J., and Beran, P. S., "Analysis of Nonlinear Aeroelastic Panel Response Using Proper orthogonal Decomposition," *Journal of Vibration and Acoustics*, Vol. 126, 2004, pp. 416–4221. doi:10.1115/1.1687389

[15] Epureanu, B. I., Tang, L. S., and Païdoussis, M. P., "Coherent Structures and Their Influence on the Dynamics of Aeroelastic Panels," *International Journal of Non-Linear Mechanics*, Vol. 39, 2004, pp. 977–991. doi:10.1016/S0020-7462(03)00090-8

[16] Xue, D. Y., and Mei, C., "Finite Element Nonlinear Panel Flutter with Arbitrary Temperatures in Supersonic Flow," *AIAA Journal*, Vol. 31, 1993, pp. 154–162. doi:10.2514/3.11332

[17] Ibrahim, H. H., Yoo, H. H., and Lee, K.-S., "Supersonic Flutter of Functionally Graded Panels Subject to Acoustic and Thermal Loads," *Journal of Aircraft*, Vol. 46, 2009, pp. 593–600. doi:10.2514/1.39085

[18] Han, A. D., and Yang, T. Y., "Nonlinear Panel Flutter Using High-Order Triangular Finite Elements," *AIAA Journal*, Vol. 21, 1983, pp. 1453–1461. doi:10.2514/3.8267

[19] Ziegler, F., *Mechanics of Solids and Fluids*, Springer, New York, 1998.

[20] Lee, J., "Comparison of the Two Formulations of $w - u - v$ and $w - F$ in Nonlinear Plate Analysis," *Journal of Applied Mechanics*, Vol. 69, 2002, pp. 547–552. doi:10.1115/1.1458556

[21] Segalman, D. J., and Dohrmann, C. R., "A Method for Calculating the Dynamics of Rotating Flexible Structures, Part 1: Derivation," *Journal of Vibration and Acoustics*, Vol. 118, 1996, pp. 313–317. doi:10.1115/1.2888183

[22] Segalman, D. J., Dohrmann, C. R., and Slavin, A. M., "A Method for Calculating the Dynamics of Rotating Flexible Structures, Part 2: Example Calculations," *Journal of Vibration and Acoustics*, Vol. 118, 1996, pp. 318–322. doi:10.1115/1.2888184

[23] Leissa, A., *Vibration of Plates*, Acoustical Society of America, New York, 1993.

[24] Reddy, J. N., *Theory and Analysis of Elastic Plates and Shells*, CRC Press, Boca Raton, FL, 2007.

[25] Hilber, H. M., Hughes, T. J. R., and Taylor, R. L., "Improved Numerical Dissipation for Time Integration Algorithms in Structural Dynamics," *Earthquake Engineering and Structural Dynamics*, Vol. 5, 1977, pp. 283–292. doi:10.1002/eqe.4290050306

[26] Hughes, T. J. R., *The Finite Element Method; Linear Static and Dynamic Finite Element Analysis*, Dover, New York, 2000.

[27] Timoshenko, S. P., and Woinowsky-Krieger, S., *Theory of Plates and Shells*, McGraw–Hill, New York, 1959.

[28] Lagarias, J. C., Reeds, J. A., Wright, M. H., and Wright, P. E., "Convergence Properties of the Nelder-Mead Simplex Method in Low Dimensions," *SIAM Journal on Optimization*, Vol. 9, 1998, pp. 112–147. doi:10.1137/S1052623496303470

[29] Beran, P. S., and Lucia, D. J., "A Reduced Order Cyclic Method for Computation of Limit Cycles," *Nonlinear Dynamics*, Vol. 39, 2005, pp. 143–158. doi:10.1007/s11071-005-1921-1

[30] Gopinath, A. K., Beran, P. S., and Jameson, A., "Comparative Analysis of Computational Methods for Limit-Cycle Oscillations," 47th AIAA/ASME/ASCE/AHS/ASC Structures, Structural Dynamics and Materials Conf., Newport, RI, AIAA Paper 2006-2076, May 2006.

[31] Doedel, E. J., Friedman, M. J., and Kunin, B. I., "Successive Continuation for Locating Connecting Orbits," *Numerical Algorithms*, Vol. 14, 1997, pp. 103–124. doi:10.1023/A:1019152611342

P. Beran
Associate Editor